Simplify your imaging workflows

Make research imaging workflows accessible, traceable, and secure with Athena Software for Core Imaging Facilities.

Thermo Scientific™ Athena Software is a premium imaging data management platform designed for core imaging facilities that support materials science research.

Athena Software ensures traceability of images, metadata, and experimental workflows through an intuitive and collaborative web interface.

Find out more at **thermofisher.com/athena**

ThermoFisher SCIENTIFIC

ADVANCED FUNCTIONAL MATERIALS
www.afm-journal.de

Decoupling the Impacts of Engineering Defects and Band Gap Alignment Mechanism on the Catalytic Performance of Holey 2D CeO_{2-x}-Based Heterojunctions

Xiaoran Zheng, Sajjad S. Mofarah,* Claudio Cazorla, Rahman Daiyan, Ali Asghar Esmailpour, Jason Scott, Yin Yao, Sean Lim, Vienna Wong, Ewing Y. Chen, Hamidreza Arandiyan, Pramod Koshy,* and Charles C. Sorrell*

Critical catalysis studies often lack elucidation of the mechanistic role of defect equilibria in solid solubility and charge compensation. This approach is applied to interpret the physicochemical properties and catalytic performance of a free-standing 2D–3D CeO_{2-x} scaffold, which is comprised of holey 2D nanosheets, and its heterojunctions with MoO_{3-x} and RuO_2. The band gap alignment and structural defects are engineered using density functional theory (DFT) simulations and atomic characterization. Further, the heterojunctions are used in hydrogen evolution reaction (HER) and catalytic ozonation applications, and the impacts of the metal oxide heteroatoms are analyzed. A key outcome is that the principal regulator of the ozonation performance is not oxygen vacancies but the concentration of Ce^{3+} and Ce vacancies. Cation vacancy defects are measured to be as high as 8.1 at% for Ru-CeO_{2-x}. The homogeneous distribution of chemisorbed, Mo-oxide, heterojunction nanoparticles on the CeO_{2-x} holey nanosheets facilitates intervalence charge transfer, resulting in the dominant effect and resultant ≈50% decrease in overpotential for HER. The heterojunctions are tested for aqueous-catalytic ozonation of salicylic acid, revealing excellent catalytic performance from Mo doping despite the adverse impact of Ce vacancies. The present study highlights the use of defect engineering to leverage experimental and DFT results for band alignment.

1. Introduction

Heterojunction nanostructures increasingly have become important owing to their advantageous properties in many technological areas, including thermocatalysis, electrocatalysis, photocatalysis, and photovoltaics.[1–5] In catalytic applications, heterojunction nanostructures leverage defect engineering as well as surface, structural, and morphological characteristics in order to enhance the performance owing to the synergism between the materials. The importance of nanoscale architecture has been highlighted by the recent emergence of the outstanding catalytic performance of nanosheets of various systems owing to the high densities of active sites deriving from their high surface areas.[6–10] State-of-the-art heterojunctions based on nanosheet-structured oxides recently have shown great promise in energy and environmental applications. However, there are only a limited number of reports of these materials since most such structures are not inherently 2D

X. Zheng, Dr. S. S. Mofarah, Dr. C. Cazorla, V. Wong, E. Y. Chen, Dr. P. Koshy, Prof. C. C. Sorrell
School of Materials Science and Engineering
UNSW Sydney
Sydney, NSW 2052, Australia
E-mail: xiaoran.zheng@unsw.edu.au; s.seifimofarah@unsw.edu.au; koshy@unsw.edu.au

Dr. C. Cazorla
Department of Physics
Polytechnic University of Catalonia
Campus Nord B4–B5, Barcelona E-08034, Spain

Dr. R. Daiyan, Dr. A. A. Esmailpour, Prof. J. Scott
Particles and Catalysis Research Group
School of Chemical Engineering
UNSW Sydney
Sydney, NSW 2052, Australia

Dr. Y. Yao, S. Lim
Electron Microscopy Unit (EMU)
Mark Wainwright Analytical Centre
UNSW Sydney
Sydney, NSW 2052, Australia

Dr. H. Arandiyan
Centre for Advanced Materials & Industrial Chemistry (CAMIC)
School of Science
RMIT University
124 La Trobe Street, Melbourne, VIC 3000, Australia

Dr. H. Arandiyan
Laboratory of Advanced Catalysis for Sustainability
School of Chemistry
University of Sydney
Sydney, NSW 2006, Australia

The ORCID identification number(s) for the author(s) of this article can be found under https://doi.org/10.1002/adfm.202103171.

DOI: 10.1002/adfm.202103171

(Table S1, Supporting Information). An alternative strategy to generate such structures is the conversion of coordination polymers (CPs) to 2D oxide nanostructures.[11] However, these often have the shortcomings of incomplete conversion and the presence of residual organic material following oxidation.[12]

In addition to morphological engineering, a second key strategy to improve the catalytic performance is defect engineering. Defect engineering at all levels can be employed with oxides through doping (0D defects), heterojunction formation (1D and 2D defects), and the introduction of multiple vacancies in the form of divacancies and clusters and mesoporosity (3D defects).[13–18] These strategies target the enhancement of the semiconducting properties through defect generation, band alignment through heterojunction establishment, and increase in active site distribution density through the introduction of new interfacial areas. While point defects are a typical result of doping, a second important potential effect is charge compensation by redox, which is facilitated by the variable valences of transition and rare earth metals. Both approaches can be used to engineer the properties and performance of catalysts. Pure CeO_{2-x} contains intrinsic $V_O^{\cdot\cdot}$ as 0D point defects owing to the easy reversibility of the Ce^{3+}–Ce^{4+} oxidation states, with an oxygen vacancy formation energy of 1.99–3.39 eV.[19] However, this value depends on the nature and concentration of the electrolyte as well as the pH of the solution.[20] In acidic media, the potential is in the range of 1.3–1.8 V.[21]

The capacity for interstitial solid solubility doping of CeO_{2-x} with cations is high owing to the large central interstice (ionic radius 0.110 nm) and the large interstice (0.160 nm) in the repulsive Ce sublattice.[22,23] However, doping also can result in the formation of secondary phases. For Mo doping, the MoO_3-CeO_2 phase diagram shows that both $Ce_2(MoO_4)_3$ and $Ce_2(MoO_3)(MoO_4)_3$ can form.[24] No solid solubilities were indicated but these were not investigated. For Ru doping, the calculated RuO_2-CeO_2 phase diagram is dominated by high-temperature spinodal decomposition; studies confirm substantial Ru solid solubility in the range 450 to 600 °C.[25,26]

CeO_{2-x} nanosheets have been applied for different catalytic applications, including thermocatalysis (CO oxidation),[27] electrocatalysis (hydrogen evolution reaction, HER),[28] and photocatalysis (air purification).[29] Improvements in the catalytic performance have been achieved through doping and heterojunction formation,[30,31] which modify the electronic band structure, thereby addressing the shortcomings of wide band gaps and short recombination times.[32] However, the doping strategies reported are based on assumptions about the types and extents of dopant solid solubility and the mechanisms of charge compensation and charge transfer. The potential for heterojunction formation is hindered in many conventional processes since charge transfer is dependent upon the establishment of chemisorption; transfer is very difficult and often impossible in physisorption.[33] Further, doping requires appropriate temperatures/times to achieve partial/complete solid solubility while heterojunction formation ideally requires chemical bond formation. Partial solubility is desired as it facilitates interphase bonding.

The present work reports outstanding catalytic performance data for CeO_{2-x} heterojunction holey nanosheets with surface doping of Mo and Ru through the introduction of midgap states and band gap realignment. The optical indirect band gaps (E_g) for the dopants in both substitutional and interstitial solid solubility as well as those of the heterojunctions themselves were calculated by density functional theory (DFT). The performance of the nanosheets was characterized by the HER in acidic environment and by catalytic ozonation of salicylic acid. The chemisorbed heterojunction Mo-CeO_{2-x} shows the best catalytic performance and excellent stability in HER (Tafel slope: 138 mV dec^{-1}) and catalytic ozonation of salicylic acid (removal efficiency: 98.5% after 60 min).

Most importantly, the work focuses on the development of mechanistic interpretations of the data in terms of the solid solubility, defect formation, charge compensation, charge transfer, electronic band modification and their effects on the sorption (HER), and active site formation (ozonation).

2. Results and Discussion

The fabrication strategy of heterojunction nanostructures has been established previously and is based on the dispersion of a flexible, stratified, cerium-based CP (CeCP), which can be transformed readily into CeO_{2-x} 2D/3D nanosheets with high oxygen vacancy concentrations ($[V_O^{\cdot\cdot}]$).[34] Cation doping of the CeO_{2-x} bulk or the surface can be affected by immersion in transition metal salt (TMS) solutions, followed by low-temperature heating that results in the controllable formation of solid solutions or transition metal oxide (TMO) heterojunction nanostructures. Details of the CeCP → CeO_{2-x} conversion are given in **Figure 1**a. According to Hume–Rothery's rules,[35] which are for close-packed metals, the prognosis and type and amount of solid solubility (and the associated defect formation and charge compensation) are enhanced by similarities in a number of factors, which are crystal structure, ionic radii, valences, electronegativities, and solubility ranges. For ceramics, the size and valence and, to a lesser extent, the electronegativity often are considered. In the present work, the relevant considerations are that 1) the rare earth Ce^{4+} is 30–50% larger than the transition metals Mo^{4+}, Mo^{5+}, Mo^{6+}, and Ru^{4+}, 2) the electronegativity of Ce is approximately half that of Mo and Ru, and 3) the cubic CeO_2 crystal structure is different from those of the dopant oxides (Table S2, Supporting Information). From the perspectives of size and structure, interstitial solid solubility would be expected for all Mo and Ru ions. From the perspective of valence, Mo^{4+} and Ru^{4+} would favor interstitial solubility but Mo^{5+} and Mo^{6+} would favor substitutional. There would be no differentiation in terms of the electronegativities.

Since the synthesis stages of the present work were done at the relatively modest conditions of 4 h at 450 °C, then the role of kinetics in the potential to achieve equilibrium is relevant. That is, although a high solid solubility may be possible, low or nil solubility may result. Further, the absence of solubility data raises the potential for the formation of undersaturated, saturated, and/or oversaturated solid solutions.[36] These issues impact on the range of adsorption mechanisms that may be exhibited by solids and heterojunction nanostructures. Figure 1b illustrates the range of such possibilities as well as some common defects that may be observed in mesoporous CeO_{2-x} nanosheets doped with cations that undergo interstitial

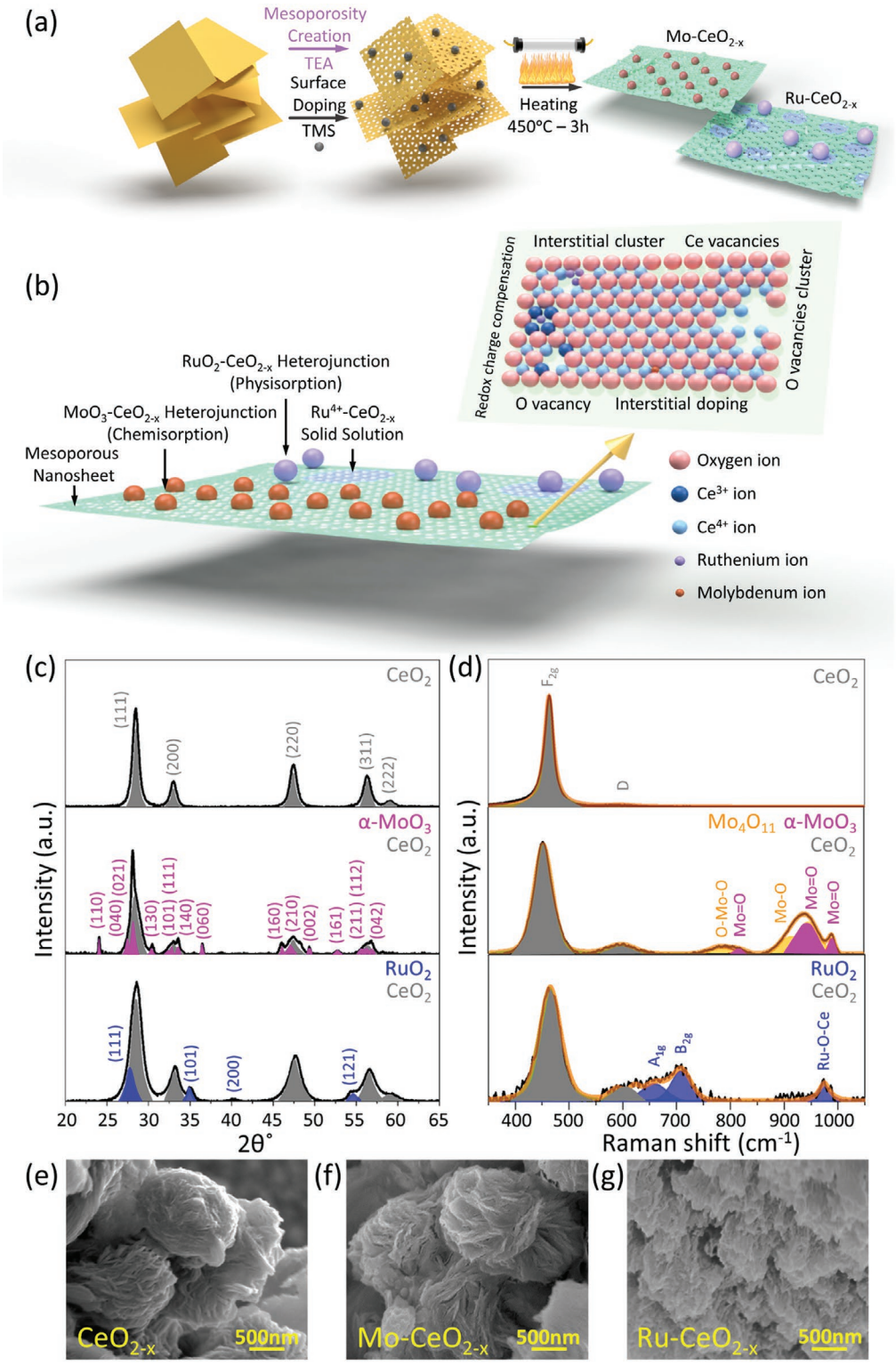

Figure 1. a) Schematic of two-step process for 1) CeCP stirred in triethanolamine (TEA) solution and transition metal salt (TMS); 2) oxidation at 450 °C in air into stacked nanosheet CeO_{2-x} heterojunction. b) Defect formation in mesoporous CeO_{2-x} nanosheets from adsorption, interstitial solid solubility, intrinsic $V_{\ddot{O}}$, and charge compensation (ionic and redox): 0D point defects, 0–2D physisorbed heterojunction interfaces, 2D chemisorbed heterojunction interfaces, 3D vacancy clusters, and 3D mesopores. c) XRD patterns (identically scaled intensities) of CeO_{2-x}, Mo-CeO_{2-x}, and Ru-CeO_{2-x}, respectively. d) Laser Raman spectra of CeO_{2-x}, Mo-CeO_{2-x}, and Ru-CeO_{2-x}, respectively; e–g) SEM images of e) CeO_{2-x}, f) Mo-CeO_{2-x}, and g) Ru-CeO_{2-x}.

solid solubility; this image reflects the experimental outcomes of the present work.

Examination of the potential defect equilibria (Tables S3–S5, Supporting Information) combined with the valence data provided by X-ray photoelectron spectroscopy (XPS) often can allow an unambiguous inference about the nature of the solid solubility mechanism. Of particular importance are 1) donor (Mo^{6+} and Mo^{5+}) and neutral (Mo^{4+} and Ru^{4+}) dopants cannot generate $V_O^{\cdot\cdot}$, 2) intervalence charge transfer (IVCT) can result in mutual valence changes between matrix and dopant cations, 3) redox charge compensation causes $Ce^{4+} \leftrightarrow Ce^{3+}$ equilibria, 4) electronic charge compensation cannot generate $V_O^{\cdot\cdot}$ or alter the $Ce^{4+} \leftrightarrow Ce^{3+}$ equilibria, and 5) defect equilibria at the surface and bulk may differ significantly. Thus, the changes in $[V_O^{\cdot\cdot}]$, $[Ce^{4+}]$, $[Ce^{3+}]$, and dopant valences provide key information about the solid solubility as well as the charge compensation required for doping.

Figure 1c,d shows the X-ray diffraction (XRD) patterns and Raman spectra, respectively, which reveal that the principal crystalline phase was CeO_{2-x}, Mo doping resulted in the detection of α-MoO_3 (XRD, Raman) and Mo_4O_{11} (Raman), and Ru doping resulted in the detection of RuO_2 (both). The presence of these secondary phases indicates probable heterojunction formation, although ≈30–35% reduction in CeO_{2-x} crystallite size (Table S6, Supporting Information) also suggests solid solubility of both dopant ions.[37] The Raman patterns (Table S7, Supporting Information) support the latter by the F_{2g} peak (464 cm^{-1}) broadening, red shift (for Mo doping), and asymmetry (for Ru doping).[38] Further, the presence of the D peak (600 cm^{-1}) is indicative of the presence of defects that may be defined as 1) $V_{Ce}^{''''} - 2V_O^{\cdot\cdot}$ Frenkel pair (ionic charge compensation);[39] 2) $2Ce_{Ce}^{'} - V_O^{\cdot\cdot}$ pair ($Ce^{4+} \rightarrow Ce^{3+}$ intrinsic redox charge compensation);[40] 3) e.g., $M_{Ce}^{\bullet} - Ce_{Ce}^{'}$ or $M_i^{\cdot\cdot\cdot\cdot} - 4Ce_{Ce}^{'}$ (extrinsic redox charge compensation);[41] or 4) e.g., $M^{5+} + Ce^{4+} \rightarrow M^{6+} + Ce^{3+}$ (IVCT), where M is a metal dopant.

Figure 1e–g shows scanning electron microscope (SEM) images that illustrate the 2D/3D flower-like nanosheets of CeO_{2-x}. With the introduction of Mo ions, the compact flower-like nanosheets become slightly exfoliated, which supports the conclusion of deposition of surface heterojunction particles and/or alteration of the surface charge through solid solubility. With the introduction of Ru ions, there is considerably more exfoliation, suggesting amplification of the effect from Ru doping.

Finer-scale morphological and structural analyses of the exfoliated heterojunction nanosheets were examined by high-resolution transmission electron microscopy (HRTEM), energy-dispersive X-ray spectroscopy (EDS), selected area electron diffraction (SAED), and atomic force microscopy (AFM), as shown in **Figure 2**. The HRTEM images (Figure 2a–c) of the three nanostructures reveal mesoporosity. The calculated pore sizes (Table S8, Supporting Information) are in the range ≈6.0–7.6 nm while the images reveal that the pore sizes are in the range ≈2–5 nm (Figure S1, Supporting Information). Further the crystallite size of CeO_{2-x} (≈8.1 nm) is larger than that of Mo-CeO_{2-x} (≈5.6 nm) and Ru-CeO_{2-x} (≈5.1 nm) (Table S6, Supporting Information) as confirmed by corresponding TEM images. The SAED patterns (Figure 2d–f) reveal that the nanostructures are slightly disordered, with the crystallinity increasing in the order Ru-CeO_{2-x} < Mo-CeO_{2-x} < CeO_{2-x}. These data are consistent with the XRD and Raman data in that they reflect increasing levels of solid solubility. The ring patterns reveal that the nanosheets consist of randomly oriented polycrystalline CeO_{2-x}, although the discrete dots in Mo-CeO_{2-x} and Ru-CeO_{2-x} indicate heterojunction formation. Consequently, there are no detectable effects of preferred orientation or associated exposed crystallographic planes on the performance. EDS mapping (**Figure 2**g–i) reveals an irregular Ce—O distribution for CeO_{2-x} indicating an inhomogenous $[V_O^{\cdot\cdot}]$ distribution; the matched Ce, O, and dopant distributions show that both doped materials exhibit homogenously distributed dopant solid solutions. The AFM data (Figure 2j–l) reveal that CeO_{2-x} forms stacked nanosheets with the examined particle thickness being ≈35.0 nm. However, the thicknesses of the individual doped nanosheets again reveal the roles of heterojunction formation and solid solubility on the recrystallization.

As confirmed by HRTEM (Figure 2m) image and EDS (Figure 2n) data, the growth and stacking of Mo-CeO_{2-x}, which was ≈1.00 nm thick from AFM (Figure 2k), were constrained by homogenously distributed, fine, chemisorbed MoO_3 heterojunction precipitates. In contrast, the growth and stacking of Ru-CeO_{2-x} were less constrained by inhomogenously distributed, coarse, physisorbed RuO_2 heterojunction precipitates (Figure 2o). Further, the ion distribution densities revealed by EDS mapping (Figure 2p) indicate that Ru exhibited bulk solubility (lower Ru distribution density with lower Ce distribution density) while Mo exhibited surface solubility (higher Mo distribution density with higher Ce distribution density). Thus, the more homogenous distribution of nucleation sites (viz., Ru ions) resulted in more ready recrystallization and consequently thicker nanosheets.

The mechanisms behind the variant dopant dispositions are shown in Figure 2q and the representative phase diagram of Figure S2 in the Supporting Information. That is, MoO_3 exhibits what is effectively surface chemisorption owing to the limited solid solubility of Mo in CeO_{2-x}, resulting in a limited but strong interfacial bonding zone between the precipitates and CeO_{2-x}. In contrast, the high solid solubility of Ru in CeO_{2-x} results in the achievement of saturation solubility of Ru in CeO_{2-x}, after which only large RuO_2 particles precipitate from solution and are weakly bonded by physisorption. These phase relations also suggest the applicability of kinetics through change in temperature to alter solid solubilities. Hence, it may be possible to obtain chemisorbed RuO_2 precipitates if the solubility is lowered by reducing the temperature to below that of the solidus.

The Raman data in Figure 1d suggest that the dopant valences across the Mo-CeO_{2-x} interface are graded and the EDS data (Figure 2n) suggest that the solubility is limited to the surface. The mechanism by which this is achieved is likely to be IVCT[42] according to Equations (1) and (2) (Table S4, Supporting Information)

$$Mo^{6+} + Ce^{3+} \rightarrow Mo^{5+} + Ce^{4+} \quad (1)$$

$$Mo^{5+} + Ce^{3+} \rightarrow Mo^{4+} + Ce^{4+} \quad (2)$$

Further, it is likely that this process is assisted by the ready transformations between the Magnéli-like Mo–O shear

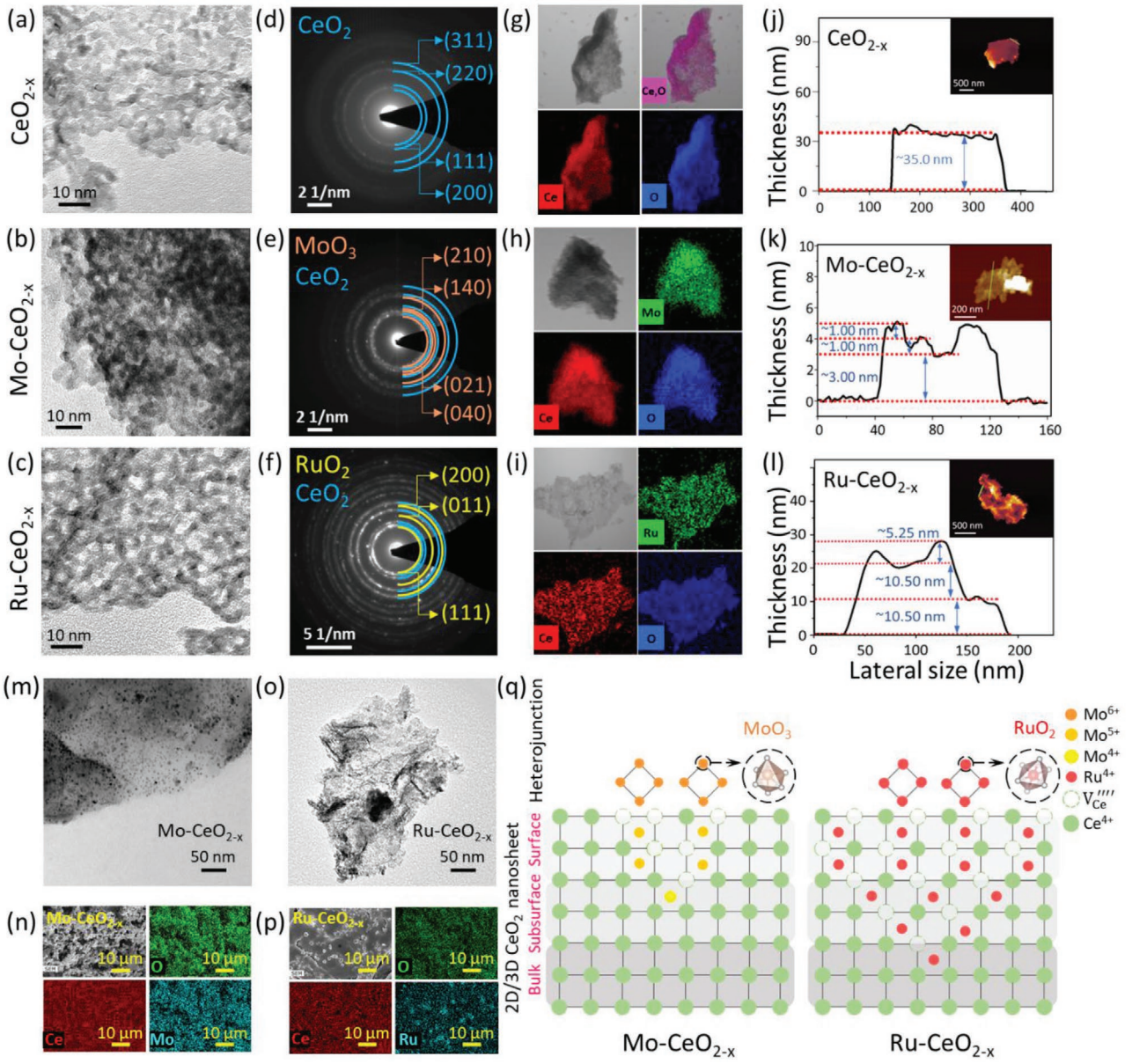

Figure 2. Characteristics of holey TMO CeO_{2-x}-based nanosheets. a–c) TEM images of holey nanosheets for: a) CeO_{2-x}; b) Mo-CeO_{2-x}; c) Ru-CeO_{2-x}, d–f) corresponding SAED images for: d) CeO_{2-x}; e) Mo-CeO_{2-x}; f) Ru-CeO_{2-x}, g–i) EDS mapping of: g) CeO_{2-x}; h) Mo-CeO_{2-x}; i) Ru-CeO_{2-x}, j–l) AFM images of j) CeO_{2-x}; k) Mo-CeO_{2-x}; l) Ru-CeO_{2-x}. Mo-CeO_{2-x}; m) TEM images of heterojunction holey nanosheets; n) EDS mapping. Ru-CeO_{2-x}: o) TEM images of heterojunction holey nanosheets; p) EDS mapping. q) Dopant solid solubilities and valences of Mo and Ru based on the present work.

structures (Figure S3, Supporting Information),[43] which also are known in the systems Ti–O,[44] Ce–O,[22] W–O,[45] and Sn–O.[46] It is considered likely that the final Mo valence is 4+ owing to its much greater stability, as suggested by its melting point of 2300 °C, than those of Mo^{5+} and Mo^{6+}, which exhibit peritectic decomposition in the temperature range 800–818 °C.

In contrast, the Raman data in Figure 1d indicate only a single Ru valence and the EDS data (Figure 2p) suggest extensive solid solubility. More broadly, interstitial solid solubility is very likely for essentially any cation owing to the very large sizes of the central interstice (0.110 nm radius) and the Ce sublattice gap (0.160 nm) through which the cation must pass. These sizes may be compared to the ionic radii (sixfold coordination only are available) of Mo^{6+} (0.073 nm), Mo^{5+} (0.075 nm), Mo^{4+} (0.079 nm), and Ru^{4+} (0.076 nm).[47]

These solid solubility characteristics are supported by the reflectance UV-vis spectra (Figure S4, Supporting Information), which are consistent with the known effect that the diffuseness of the overall spectra reflects the extent of defect concentration.[47] Hence, the sharpest pattern is for CeO_{2-x}, the pattern for Mo-CeO_{2-x} is only slightly more diffuse owing to the isolation of the Mo ions in the surface and subsurface, but the pattern for Ru-CeO_{2-x} is highly diffuse owing to the extensive solid solubility of the Ru ions in the bulk.

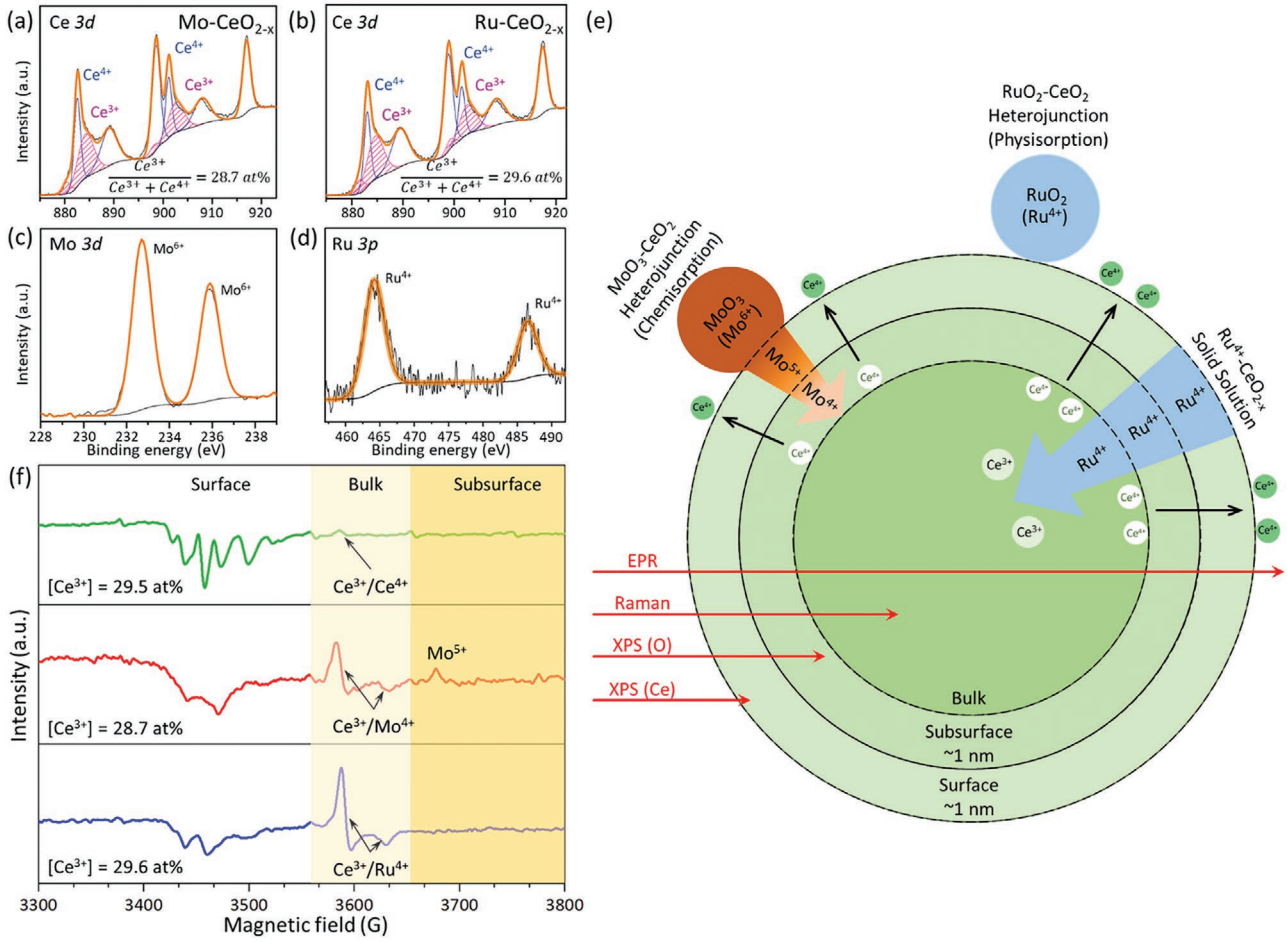

Figure 3. Defect analysis of TMO in 2D/3D heterostructures: a,b) XPS spectra for Ce 3*d* orbital of the Mo-CeO_{2-x} and Ru-CeO_{2-x}, respectively; c,d) XPS spectra for Mo 3*d* orbital of the Mo-CeO_{2-x} and for Ru 3*p* orbital of Ru-CeO_{2-x}; e) schematic of heterojunction formation, solid solubility, and charge compensation mechanisms based on data in Tables S3 (Supporting Information, heterojunction defect equilibria), Table S4 (Supporting Information, graded defect equilibria), and Table S9 (Supporting Information, XPS data interpretation). f) EPR spectra of the CeO_{2-x}, Mo-CeO_{2-x}, Ru-CeO_{2-x}, respectively (nonidentical intensity scales).

The chemical and defect analyses of the heterojunction nanostructures undertaken by surface XPS is shown in **Figure 3**a–d. The relative atomic concentrations of the two oxidation states Ce^{3+} and Ce^{4+} were obtained by deconvolution of the 3*d* orbital spectra into discrete peaks using Gaussian fitting (Figure S5, Supporting Information).[48] Figure 3c reveals two discrete peaks at 235.9 and 232.7 eV, which are assigned to the Mo $3d_{3/2}$ and Mo $3d_{5/2}$ orbitals of Mo^{6+}, respectively. The Ru 3*d* peaks are problematic owing to overlap with the C 1s peaks from adventitious carbon.[49] Consequently, the Ru $3p_{3/2}$ and Ru $3p_{5/2}$ peaks are used for quantitative analysis. Figure 3d shows peaks at 464.3 and 485.9 eV, which are characteristic of the Ru $3p_{3/2}$ and Ru $3p_{5/2}$ peaks of Ru^{4+}, respectively. The complete XPS data for CeO_{2-x}, Mo-CeO_{2-x}, and Ru-CeO_{2-x} are given in **Table 1** and these data are interpreted in Table S9 in the Supporting Information.

The nature of the solid solubility mechanism can be elucidated by consideration of the XPS data in conjunction with the defect equilibria:

1) *Mo^{4+} Solid Solubility*: The data in Table 1 show that the changes in the concentrations do not allow differentiation between substitutional and interstitial solid solubilities.
2) *Mo^{5+} and Mo^{6+} Solid Solubility*: These donor dopants could exhibit maximal Mo solubility of 4.1 at% (Table 1). Substitutional solid solubility in ionic charge compensation (Tables S3 and S5, Supporting Information) occurs at Mo/V_{Ce}'''' ratios of 4.00 and 2.50, respectively, which would result in maximal [V_{Ce}''''] of 1.03 and 0.63 at%, respectively. In contrast, interstitial solid solubility and ionic charge compensation (Tables S3 and S4, Supporting Information) involve Mo/V_{Ce}'''' ratios of 0.80 and 0.75, respectively, which would result in maximal [V_{Ce}''''] of 5.13 and 5.47 at%, respectively. Table 1 shows that the [V_{Ce}''''] calculated from the change in [Ce] upon Mo doping is 3.1 at%. Since the maximal solubility is unlikely to have been achieved, then substitutional solubility is not possible and the resultant interstitial solubility, accompanied by ionic charge compensation, of Mo is ≈2.4 at% $\left(3.1\,\text{at\%} \times \left[\frac{0.80+0.75}{2}\right]\right)$. However, this is likely to be affected by the probable concentration of the dopant at this low concentration on the surface and subsurface of the particle.
3) *Ru^{4+} Solid Solubility*: This neutral dopant shows completely different behavior from that of Mo. Table 1 shows that the total [Ce] decreased and the [Ce^{3+}] in the bulk increased

Table 1. Detailed comparative analysis of XPS parameters for CeO_{2-x}, Mo-CeO_{2-x}, Ru-CeO_{2-x}.

Row	Parameter [at%]	Location	CeO_{2-x}	Mo-CeO_{2-x}	Ru-CeO_{2-x}
1	Ce Concentration (at%)	Total Volume	27.7	24.6	19.5
2	$[V_{Ce}^{''''}]_{Theoretical}$ (at%)	Total Volume	0.0	3.1	8.2
3	O Concentration (at%)	Total Volume	67.3	67.5	67.8
4	Ce/O Ratio	Total Volume	0.41	0.36	0.28
5	O/Ce Ratio	Total Volume	2.43	2.74	3.48
6	O/(Ce + X) Ratio	Total Volume	2.43	2.50	2.58
7	Ce/(Ce + O) Concentration	Total Volume	29.2	26.7	22.3
8	$Ce^{3+}/(Ce^{3+} + Ce^{4+})$ Concentration	Surface	29.5	28.7	29.6
9	$O\text{-}Ce^{3+}/O\text{-}Ce^{4+}$ Concentration	Bulk	20.3	19.7	38.4
10	$O\text{-}Ce^{3+}/(O\text{-}Ce^{3+} + O\text{-}Ce^{4+})$ Concentration	Bulk	16.9	16.5	27.7
11	Hypothetical $V_O^{\cdot\cdot}$ Concentration (at%)	Surface	14.8	14.4	14.8
12	Hypothetical $V_O^{\cdot\cdot}$ Concentration (at%)	Bulk	8.5	8.3	13.8
13	Added Dopant Concentration (at%)	–	0.0	4.1	6.8

significantly. If Ru dissolves substitutionally, the [Ce] would decrease but there would be no impact on the $[Ce^{3+}]$. However, the defect equilibria in Table S4 in the Supporting Information show that interstitial solid solubility would result in the formation of $V_{Ce}^{''''}$, thus involving ionic charge compensation, but that redox charge compensation would increase the $[Ce^{3+}]$. Consequently, it is clear that Ru exhibits interstitial solid solubility. Further, the maximal Ru solubility is 6.8 at% (Table 1) and interstitial solid solubility (Table S4, Supporting Information) involves the Ru/$V_{Ce}^{''''}$ ratio of 1.00, which would result in maximal $[V_{Ce}^{''''}]$ of 6.80 at%. The $[V_{Ce}^{''''}]$ calculated from the change in [Ce] upon Ru doping is 8.2 at% (Table 1), this indicates that the dopant is concentrated at the surface, exhibiting the expected diffusion gradient into the bulk. This is an unavoidable result of the penetration depth limitation of XPS for CeO_2 of 1–3 nm and the particle size of ≈5 nm (Tables S1 and S6, Supporting Information).[22] However, these data suggest that all of the dopant has dissolved, so the saturation solid solubility would be ≥6.8 at%. In contrast with Mo doping, the higher overall concentration of the dopant is consistent with volumetric solid solubility.

Concerning the data in Table 1 and Table S9 in the Supporting Information, values of O/Ce > 2.0 for CeO_{2-x} have been observed before,[50] reaching as high as 2.8 in the bulk[51] and 3.15 at the surface,[52] although it is uncommon for researchers to report these data. The reason for the oxygen hyperstoichiometry is the greater penetration depth of the beam for oxygen detection compared to that for cerium detection.[53] A critical point is the approximately constant oxygen concentrations in Table 1, which clarify why it is not possible for interdependent substitutional solid solubility, ionic charge compensation, and $V_O^{\cdot\cdot}$ formation to be applicable. The reason for this is that the oxygen concentrations ([O]) are approximately constant (although they actually increase from 67.3 to 67.5 to 67.8 at% upon doping) while the cerium concentrations ([Ce]) decrease significantly (from 27.7 to 19.5 at%). In fact, calculations of the other ionic ratios are consistent in demonstrating increasing [O], which is consistent with $V_O^{\cdot\cdot}$ annihilation, which results from the charge compensation for donor doping. These phenomena are explained unambiguously by interdependent interstitial solid solubility, ionic (Mo) or ionic plus redox (Ru) charge compensation, and $V_{Ce}^{''''}$ formation. Thus, the formation of $V_O^{\cdot\cdot}$ plays no role in the equilibria.

The XPS identification of Mo^{6+}, Raman (and subsequent electron paramagnetic resonance (EPR)) identification of Mo^{5+}, relative stabilities ($Mo^{6+} > Mo^{4+} > Mo^{5+}$),[43] solid solubility considerations (viz., Hume–Rothery's rules),[35] the Magnéli-like Mo–O structures, and IVCT considerations all suggest that the Mo/CeO_{2-x} interface is likely to be graded. The XPS data demonstrate interstitial solid solubility and ionic charge compensation, the corresponding defect equilibria across the heterojunction interface, surface, and subsurface are shown in Equations (3)–(5)

Interface

$$3Mo_{Mo}^{x} + 9O_O^{x} \xrightarrow{CeO_2} Mo_i^{\cdot\cdot\cdot\cdot\cdot\cdot} + 2Mo_i^{\cdot\cdot\cdot\cdot\cdot} + 4V_{Ce}^{''''} + 4Ce_S^{x} + 9O_O^{x} \quad (3)$$

Surface

$$4Mo_{Mo}^{x} + 10O_O^{x} \xrightarrow{CeO_2} 4Mo_i^{\cdot\cdot\cdot\cdot\cdot} + 5V_{Ce}^{''''} + 5Ce_S^{x} + 10O_O^{x} \quad (4)$$

Subsurface

$$Mo_{Mo}^{x} + 2O_O^{x} \xrightarrow{CeO_2} Mo_i^{\cdot\cdot\cdot\cdot} + V_{Ce}^{''''} + Ce_S^{x} + 2O_O^{x} \quad (5)$$

Since the $[Ce^{3+}]$ is unchanged at the surface but it is present in the bulk, then the greater proximity of the ions in the subsurface and bulk relative to that at the surface indicates:

Graded bonding					IVCT	
Mo^{6+}	→	$Mo^{6+} + Mo^{5+}$	→	$Mo^{5+} + Ce^{3+}$	↔	$Mo^{4+} + Ce^{4+}$
Adsorbate		*Interface*		*Surface*		*Subsurface*

As mentioned, the XPS data for Ru-CeO_{2-x} indicate that, although Ru dissolves interstitially, the [Ce] decreases, and the [Ce^{3+}] increases. This is explained by the simultaneous presence of both ionic and redox charge compensation mechanisms, which are represented by Equation (6)

$$\text{All levels}: 2Ru_{Ru}^{x} + 4O_{O}^{x} \overset{CeO_2}{\rightarrow} 2Ru_{i}^{\cdots\cdot} + V_{Ce}^{''''} + Ce_{S}^{x} + 4O_{O}^{x} + 4Ce_{Ce}^{'} \quad (6)$$

These solid solubility and charge compensation mechanisms, which are derive largely from the XPS data, are illustrated in Figure 3e.

The confirmation of solid solubility through consideration of the nature of the defects was examined by EPR spectroscopy at room temperature, as shown in the full spectra in Figure S6 in the Supporting Information and the enlargements are shown in Figure 3f. The *g* factors calculated from these spectra are given in Table S10 in the Supporting Information, which differentiates between literature assignments and assignments based on the present work.

When the *g* factor is <2.0023, the electrons have low mobilities and so these defects are localized.[54,55] The signal at *g* = 1.967 (3589 G) represents Ce^{4+}/Ce^{3+} redox species at the surface, which result from the trapping of electrons in the oxygen vacancies. Figure S6 in the Supporting Information reveals that, upon the introduction of either dopant, this signal is strengthened, which is attributed to the Ce^{4+}/Ce^{3+} redox resulting from the interstitial solid solubility of the dopant, $V_{Ce}^{''''}$ formation, and ionic and redox charge compensation. It can be seen that the intensities increased in the order CeO_{2-x} < Mo-CeO_{2-x} < Ru-CeO_{2-x}, which is consistent with the relative amounts of dopants (nil < surface < bulk). More importantly, the observation that both dopants enhance the same peak indicates that the mechanism to create unpaired electrons is the same. Since neutral Ru^{4+} clearly dissolves interstitially in the bulk, then this shows that neutral Mo^{4+} also dissolves interstitially in the subsurface (which is equivalent to the bulk; see footnote to Table S10, Supporting Information). This is significant because it confirms the presence of Mo^{4+} as the terminating layer in the graded surface. Since surfaces have higher energies than the bulk,[56] the *g* factors have been differentiated between surface and bulk phenomena. Consequently, although *g* factor for Mo^{5+} has been identified,[57] this can be assigned to the surface since it is not present in the bulk, as shown in Figure 3f. Similarly, there is no *g* factor for Mo^{6+} because this valence does not bond with CeO_{2-x}. Finally, there are *g* factors for both surface and bulk Ru^{4+} because it is present in both regions.

In contrast, when the *g* factor is > 2.003, as given in Table S10 in the Supporting Information, this indicates a signal from $^{\bullet}O_2^-$, which results from the reaction initiated by EPR in Equation (7)

$$Ce^{3+} + O_2 \rightarrow Ce^{4+} - {}^{\bullet}O_2^- \quad (7)$$

The indicated oxygen vacancies are oxygen adsorption centers that can be classified as individual or clustered. Importantly, the oxygen is adsorbed into an oxygen vacancy, so the EPR signal represents an indirect measure of [$V_O^{\cdot\cdot}$]. In effect, Equation (7) can be revisualized as Equation (8)

$$\left\{2Ce^{3+} + V_O^{\cdot\cdot}\right\} + \left\{Ce^{3+} + O_2\right\} \rightarrow \left\{2Ce^{4+}\right\} + \left\{Ce^{4+} - {}^{\bullet}O_2^-\right\} \quad (8)$$

Hence, a single $V_O^{\cdot\cdot}$ is converted to a single $^{\bullet}O_2^-$. However, Table S10 in the Supporting Information shows that two *g* factors previously were assigned for Ce^{3+}.[58] In the present work, these have been harmonized with Equation (8) by assigning these to the other member component, which is Ce^{3+} + O_2. Consequently, these *g* factors have been assigned by adsorbed oxygen in proximity to Ce^{3+}.

Figure S6 in the Supporting Information also shows that the EPR signal intensities for *g* factors > 2.0023 were in the order Mo-CeO_{2-x} < Ru-CeO_{2-x} < CeO_{2-x}. This trend is interpreted in terms of Equation (8), which suggests the relative [$V_O^{\cdot\cdot}$] for the three samples. That is, in contrast to the proposed defect equilibria, which are based on dopant interstitial (i.e., donor dopant) solid solubility and combined ionic and redox charge compensations, an alternative charge compensation mechanism associated with the presence of intrinsic Ce^{3+} and $V_O^{\cdot\cdot}$ in CeO_{2-x} may occur. Using Ru-CeO_{2-x} as the example, the elaborate defect equilibria for dopant and matrix would be Equations (9) and (10)

Ionic charge compensation

$$\left[Ru_{Ru}^{x}\right] + \left[4C_{Ce}^{'} + 8O_{O}^{x} + 2V_{O}^{\cdot\cdot} + O_2(g)\right] \overset{CeO_{2-x}}{\rightarrow} \left[Ru_{i}^{\cdots\cdot}\right] + \left[4Ce_{Ce}^{'} + 8O_{O}^{x}\right] \quad (9)$$

Electronic charge compensation

$$\left[Ru_{Ru}^{x}\right] + \left[4Ce_{Ce}^{'} + 8O_{O}^{x} + 2V_{O}^{\cdot\cdot} + O_2(g)\right] \overset{CeO_{2-x}}{\rightarrow} \left[Ru^{\cdots\cdot}{}_{i}\right] + \left[4Ce_{Ce}^{x} + 8O_{O}^{x} + 4e'\right] \quad (10)$$

Consequently, Mo-CeO_{2-x} exhibits the lowest effect since the solubility is limited to the surface, Ru-CeO_{2-x} exhibits a greater effect owing to its bulk solubility, and CeO_{2-x} has the greatest effect because the [$V_O^{\cdot\cdot}$] was highest since oxygen vacancy annihilation does not occur. Finally, since Table 1 shows that that [Ce^{3+}] was constant for all three samples, then Equation (9) governs, and not Equation (10) since the latter involves $Ce^{3+} \rightarrow Ce^{4+}$ oxidation.

Photoluminescence (PL) spectra arise from the presence of point defects that generate energy transitions between ground and excited states associated with luminescent centers, which often are color or F centers,[59] where the peak intensities are inversely proportional to the rates of electron–hole recombination. This effect generally is controlled by the diffusion distance (i.e., particle size), the presence of trap states (i.e., defects), and the presence of heterojunctions (i.e., interfaces). **Figure 4**a shows the PL data for the samples and the attributed transitions, most of which are associated with the color centers F^0 ($V_O^{\cdot\cdot}$), F^+ ($V_O^{\cdot}$), and F^{++} (V_O^{x}) and these are summarized in Table S11 in the Supporting Information. Aškrabić et al.[60] have proposed the most thorough assessment of the PL data for CeO_{2-x} at an excitation wavelength of 325 nm from 15 K to room temperature. These data are interpreted principally in terms of the excitation energies associated with all three types

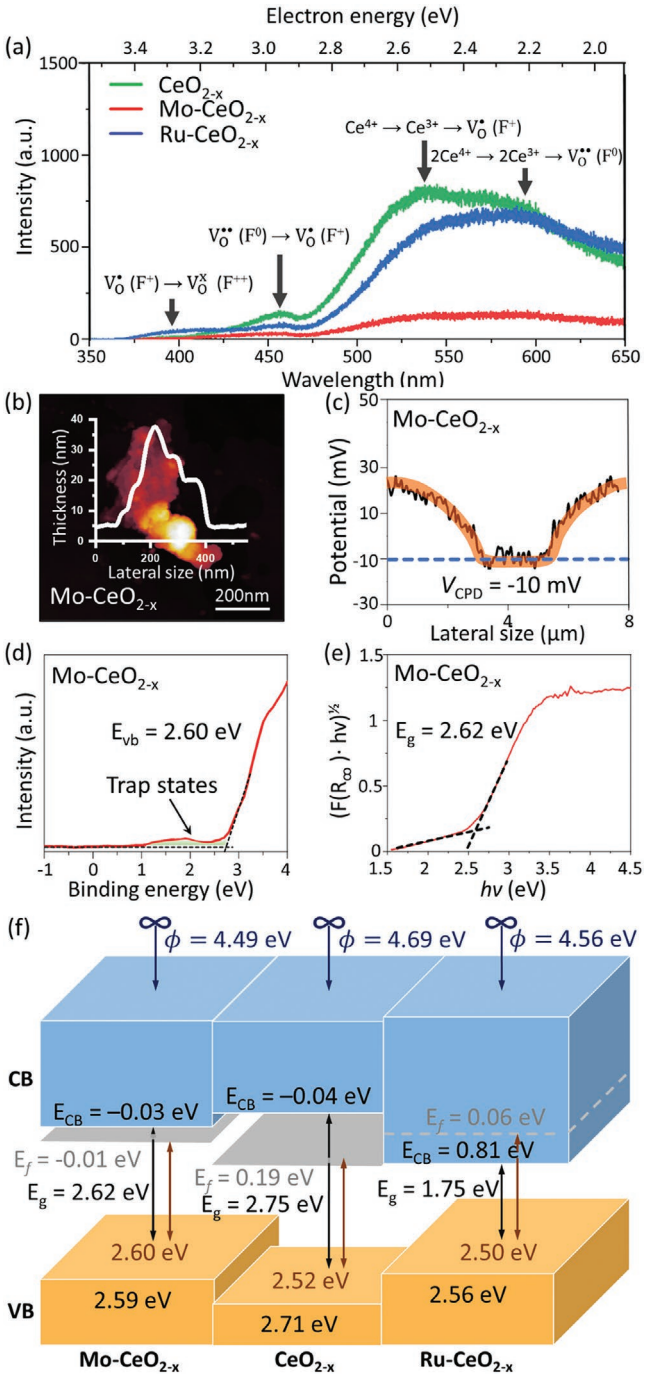

Figure 4. Band structure characteristics of CeO_{2-x} and 2D/3D heterostructures: a) PL spectra of the CeO_{2-x}, Mo-CeO_{2-x}, and Ru-CeO_{2-x}. b) Topography of Mo-CeO_{2-x} holey nanosheet by KPFM imaging; c) contact potential difference measured by KPFM of Mo-CeO_{2-x} holey nanosheet; d) XPS valence band plot for Mo-CeO_{2-x} holey nanosheet; e) Kubelka-Munk plot from UV-vis reflectance spectrophotometry data for optical indirect band gap of Mo-CeO_{2-x} holey nanosheet. f) Energy band diagrams (pH = 0).

of F centers. Table S11 in the Supporting Information reveals a reasonable correlation between the peak positions for the samples, which were fabricated by precipitation and self-propagating synthesis and those for the samples of the present work, which were fabricated by electrodeposition to produce a CP, followed by oxidation.[61] However, an aspect of PL that does not appear to have been considered is the potential for the formation and transition between color centers, the energies of which are associated with the formation of midgap states.[62] Consequently, speculative alternative assignments for the major PL peaks are proposed in Table S12 in the Supporting Information.

These alternative assignments suggest that the PL data reflect the effect of increasing energy on the formation sequence of defects (Equation (11)) and the transitions between the defect states (Equations (12) and (13))

$$2Ce^{4+} \rightarrow Ce^{3+} + (Ce^{3+} + V_O^{\bullet\bullet}) \rightarrow Ce^{3+} + (Ce^{4+} + V_O^{\bullet}) \rightarrow Ce^{4+} + (Ce^{4+} + V_O^{x}) \quad (11)$$

$$Ce^{3+} + V_O^{\bullet\bullet} \rightarrow Ce^{4+} + V_O^{\bullet} \quad (12)$$

$$Ce^{3+} + V_O^{\bullet} \rightarrow Ce^{4+} + V_O^{x} \quad (13)$$

Figure 4a shows that the (beneficial) inverse intensities exhibit a general trend of CeO_{2-x} < Ru-CeO_{2-x} < Mo-CeO_{2-x}. Table S1 in the Supporting Information reveals a direct correlation with the nanosheet thickness (1–3 < 5 < 35 nm) but Table S6 in the Supporting Information shows that the crystallite size does not (5.1 > 5.6 < 8.1 nm). These results are consistent with effects from the heterojunctions and the defects. That is, for the two low-energy PL peaks, the chemisorbed heterojunction of Mo-CeO_{2-x} is more effective than the physisorbed heterojunction of Ru-CeO_{2-x} in facilitating the directional diffusion of the electrons (where these interstitial dopants are donors and hence cause n-type conductivity). These heterojunctions would allow some of the charge carriers to circumvent the potential deep trapping states arising from the dopant defects and F centers. While the easy Ce^{4+}/Ce^{3+} redox switching suggests a low driving force for electron trapping, the F centers in CeO_{2-x} represent defects with very strong driving forces to trap electrons, especially V_O^{x}. Consequently, the significant decreases in the PL intensities for the two high-energy transitions are attributed to transitions to the F^{+} ($V_O^{\bullet}$) and F^{++} (V_O^{x}) centers, which represent effective trapping sites. Although this appears to be counter-intuitive, this effect derives not from trapping per se but from the effect of the F centers on the band alignment, where it is known that the E_f can be raised significantly by F centers, even to an energy above that of the conduction band minimum (CBM).[63] Consequently, when electrons are trapped near or above the CBM, most of the electrons are conducting and hence have high mobilities.

The energy band diagrams were calculated using the data from Kelvin probe force microscopy (KPFM), valence band XPS, and reflectance UV-vis, which yielded E_f (from the contact potential difference, CPD, and resultant work function, φ, 4.69 eV for pure CeO_2),[64] the distance from the valence band (VB) to the E_f, and the optical indirect band gap (E_g), respectively. The equivalent data for CeO_{2-x} (Figure S7, Supporting Information), Mo-CeO_{2-x} (Figure 4b–e and Figure S8, Supporting Information), and Ru-CeO_{2-x} (Figure S9, Supporting

Information) are provided. The resultant energy band diagrams for CeO_{2-x}, Mo-CeO_{2-x}, and Ru-CeO_{2-x} are shown in Figure 4f.

Based on analogy with Ce-doped TiO_2,[14] these calculations show the following:

1) The E_g values of the heterojunction systems are significantly less than that of CeO_{2-x}.
2) The E_f for Mo-CeO_{2-x} is raised near the CBM.
3) The E_f for Ru-CeO_{2-x} is above the CBM.
4) The E_f values are, as mentioned previously, consistent with the effect of the F centers.
5) As the E_f values for the F centers increase in energy in the order $V_O^{\cdot\cdot} < V_O^{\cdot} < V_O^{x}$, then it is likely that the major effect derives from the F^{++} center.
6) Similarly, the role of oxygen vacancies would be unlikely to be important as this is the most likely to be a deep trapping site.
7) The lowering of the CBM values also is consistent with the greater populations of the energy levels immediately below and above the CBM values owing to the shifts in the E_f values. The role of metal interstitials also may be relevant as these would exhibit energy levels near the CBM. However, the PL data show that this effect is unlikely since Mo-CeO_{2-x}, with limited solubility, showed the greatest effect.
8) Conversely, the role of interstitials may be altered by IVCT since decreasing the valence causes an increase in the energy level toward the CB.
9) The slight lowering of the VBM for Mo-CeO_{2x} is consistent with the raising of the E_f.
10) However, the slight raising of the VBM for Ru-CeO_{2-x} is not consistent with the raising of the E_f, which suggests the population of a low-energy midgap state. This effect is most likely to be from $V_{Ce}^{''''}$, the values of which would tend to be close to the VBM.
11) For Mo-CeO_{2-x}, the CBM (–0.03 eV) is proximity to the redox potential $^{\cdot}H/H_2$ (0.00 eV).[65] The lowered E_g relative to pure CeO_{2-x} indicates that this heterojunction would be suitable for photocatalytic water splitting.

First-principles calculations based on DFT were performed in order to characterize further the differences in electronic band structures between CeO_2 and Mo and Ru ions in interstitial sites. Schematics of the electronic densities of states are shown in **Figure 5**a–f and the optical indirect band gaps obtained from these data are given in Table S13 in the Supporting Information. The correlation between the experimental and calculated E_g values for interstitial (Figure 5) versus substitutional (Figure S10, Supporting Information) solid solubility for Ru-CeO_{2-x} support the conclusion that the solid solubility mechanism is interstitial; the data for Mo-CeO_{2-x} are less conclusive. However, the close correlation for interstitial Mo^{6+} suggests that there may be some solid solubility of this ion in the surface, which is not indicated in Figure 3e.

Based on the DFT simulations, a schematic of the electronic band energy modifications for the Mo-CeO_{2-x} and Ru-CeO_{2-x} systems are shown in Figure 5g. In the chemisorbed MoO_3-CeO_2 heterojunction structure (Figure 5a), the CB electrons tend to migrate from CeO_2 to MoO_3 since MoO_3 has a smaller band gap (2.0 eV)[66] and the VB position did not show any charge transfer between them, which probably is due to the common anion rule. The Mo^{6+} ions, which exhibit limited interstitial solid solubility at the interfacial surface, are shallow electron traps (Figure 5d), being close to the VB position. This can result in VB offset, which increases the likelihood of hole transfer from MoO_3 to CeO_2 to promote electron/hole separation; it also effectively reduces the E_g. Hence, these phenomena are consistent with a type II heterojunction. The greater interstitial solid solubilities of Mo^{5+} (surface) and Mo^{4+} (subsurface) give rise to a number of deep defect states in the band gap (Figure 5e,f). As these act as electron traps and CeO_2 is an n-type semiconductor, they would not be beneficial to the catalytic performance. However, the graded Mo^{5+} and Mo^{4+} provide a chemically bonded anchor for the MoO_3, which is facilitated by IVCT.

The RuO_2 has a very narrow E_g (0.47 eV).[67] In the physisorbed RuO_2-CeO_2 heterojunction structure (Figure 5b), the CB electrons would be driven to migrate from CeO_2 to RuO_2 since RuO_2 has a very small band gap. However, the weak physisorbed bond would be likely to preclude a significant proportion of this conductivity. The Ru^{4+} ions, which exhibit extensive interstitial solid solubility into the bulk, are relatively shallow electron traps (Figure 5d). Hence, these phenomena are consistent with a type I heterojunction. As these midgap states are present in proximity to both the CB (donor) and VB (acceptor), they could aid in charge separation. Further, the midgap Ru 4*d* band partially overlaps with Ce 4*f* band, which causes band tail state formation, which effectively lowers the E_g.[68]

The experimental E_g of 2.73 eV is considerably less than the typical literature value of 3.00 eV[69] and less than the value of 3.2 eV calculated by DFT (Figure S10, Supporting Information). According to Xu et al.,[22] the E_g can be calculated on the basis of the $[V_O^{\cdot\cdot}]$ according to a linear relationship. However, the present work demonstrates that the $[V_O^{\cdot\cdot}]$, which is calculated from the $[Ce^{3+}]$, does not correlate with the $[Ce^{3+}]$ owing to redox charge compensation. Consequently, the reported equation has been converted to utilize the bulk $[Ce^{3+}]$ in Equation (14)

$$E_g = 3.0 - 1/2\left(0.032 \times \left[O - Ce^{3+}\right]\right) \quad (14)$$

Using this equation and the $[O–Ce^{3+}]$ of 16.9 at% (Table 1), the calculated E_g is 2.73 eV, which is an exact match. This outcome suggests that, for pure CeO_{2-x}, determination of the bulk $[Ce^{3+}]$ (i.e., $[O–Ce^{3+}]$) by XPS and use of Equation (14) can provide an accurate determination of the E_g. Clearly, the narrowing of the E_g does not derive from the widely perceived effect of the $[V_O^{\cdot\cdot}]$ but from the more reliable effect of $[Ce^{3+}]$, where the unreliability of the former derives from the potential for charge compensation mechanisms other than those that are purely ionic (viz., redox, IVCT, and electronic).

Defect engineering and band gap alignment are two key strategies to improve catalytic performance. The present work explores the diversity of the ceria-based materials in terms of catalytic application, and it highlights the different beneficial relationships that can be established between dopants and the ceria defects. The two distinct catalytic systems examined are: 1) water splitting through the electrocatalytic HER and 2) water purification via heterogenous catalytic ozonation. In the former case, the associated polarization curves in **Figure 6**a reveal

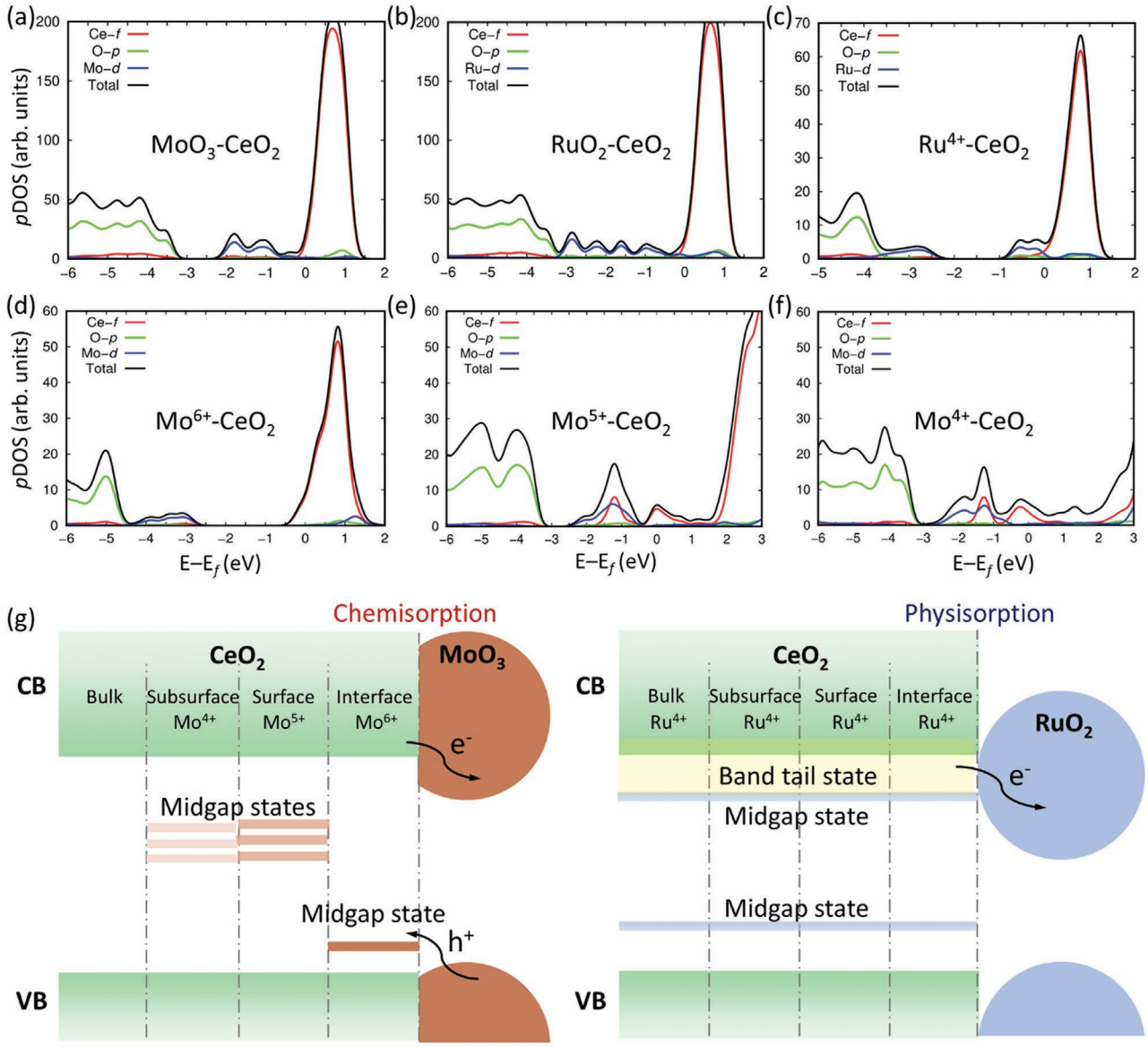

Figure 5. First-principles DFT simulations of electronic densities of states and optical indirect band gaps of: a) MoO_3-CeO_2 heterojunction nanostructure; b) RuO_2-CeO_2 heterojunction nanostructure; c) Ru^{4+}-CeO_2 interstitial solid solution; d) Mo^{6+}-CeO_2 interstitial solid solution; e) Mo^{5+}-CeO_2 interstitial solid solution; f) Mo^{4+}-CeO_2 interstitial solid solution; g) schematic of electronic band energy modification of CeO_2 from Mo or Ru doping and MoO_3-CeO_2 and RuO_2-CeO_2 heterojunction formation.

that the incorporation of Mo and Ru into CeO_2 significantly increases the current density (j) in acidic environments in the order Mo-CeO_{2-x} > Ru-CeO_{2-x} > CeO_{2-x}. Mo-CeO_{2-x} attains a j of 10 mA cm^{-2} at 315 mV of overpotential whereas Ru-CeO_{2-x} and CeO_{2-x} require respective additional 60 and 275 mV overpotential in order to reach the same j (Figure 6b). The HER performances of the samples are compared to those of commercial MoO_3 and RuO_2, as shown in Figure 6a and Figure S11 in the Supporting Information. These data are very informative in that the intrinsic poor performance of CeO_{2-x} and MoO_3 and outstanding performance of Mo-CeO_{2-x} are associated with the effect of the chemisorbed heterojunction, where the difference resulting from the absence (CeO_{2-x}) and presence (Mo-CeO_{2-x}) of the chemisorbed heterojunction is delineated clearly. In contrast, the comparison between the data for RuO_2 and Ru-CeO_{2-x} clearly shows the superior HER performance of RuO_2 and the poorer performance of Ru-CeO_{2-x}. In this case, the reduced effect of the physisorbed heterojunction could be compensated by the enhanced effect of the relatively large heterojunction particles located on the CeO_{2-x} nanosheets (Figure 2n). Finally, the superior performance of Mo-CeO_{2-x} compared that that of Ru-CeO_{2-x} can be attributed to the differences in interfacial bonding and the associated ease of charge transfer. The HER kinetics for the catalysts also were determined and are shown in the Tafel plot of Figure 6c. A similar trend is observed, where Mo-CeO_{2-x} exhibits the lowest Tafel slope (138 mV dec^{-1}). Although the Tafel slopes exhibited by the heterojunction catalysts are below those of benchmark Pt-based

catalysts of 30 mV dec^{-1},[70] the Mo-CeO_{2-x} outperforms other CeO_{2-x}-based catalysts (Table S14, Supporting Information). The performance can be improved by altering the dopant levels by increasing the solid solubility by increasing the calcining temperature, decreasing the solid solubility by decreasing calcining temperature, or altering the atmosphere to manipulate the defect equilibria and charge compensation mechanisms. The comparatively poor HER performance by pure CeO_{2-x} results from its inherent property deriving from its strong adsorption capacity toward hydrogen.

It is common for the catalytic performance to be assessed in terms of the $[V_O^{\cdot\cdot}]$,[71] which are considered to be active sites. However, the minority opinion also considers that $V_{Ce}^{''''}$ are active sites.[72] In the present work, Tables S9 and S14 in the Supporting Information reveal that the Tafel slopes do not correlate with the surface $[V_O^{\cdot\cdot}]$, bulk $[V_O^{\cdot\cdot}]$, $[V_{Ce}^{''''}]$, surface $[Ce^{3+}]$ or bulk $[Ce^{3+}]$. Further, the Tafel slopes do not correlate with the Brunauer–Emmett–Teller (BET) surface areas (Table S8, Supporting Information). Consequently, it is apparent that the nature of the heterojunctions is responsible for the observed HER behavior. The valence-graded Mo-CeO_{2-x} interface would enhance the directional diffusion of charge carriers, facilitate charge separation, enable robust heterojunction formation, improve charge transfer between phases, enhance IVCT, and prevent restacking of the nanosheets, all of which would contribute to optimization of the HER performance. In contrast, the Ru-CeO_{2-x} interface, which forms a weakly bonded physisorbed heterojunction, would be much less effective as a charge-transfer medium as it lacks most of the preceding characteristics. Consequently, the absence of heterojunction formation in CeO_{2-x} would be expected to result in the worst HER performance, which is in agreement with prior reports in the literature. Although these considerations involve a number of variables, it is clear the nanojunction formation is critical. Beyond this, it is possible to quantify the effect of restacking of the nanosheets with the resultant thicknesses provided in Table S1 in the Supporting Information which shows that the measured thicknesses were in the order Mo-CeO_{2-x} (1–3 nm) < Ru-CeO_{2-x} (5 nm) < CeO_{2-x} (35 nm), which matches with the HER performances and the respective Tafel slopes of 138, 241, and 375 mV dec^{-1}, as shown in Figure 6b.

These phenomena can be interpreted similarly by the electrochemical impedance spectroscopy (EIS) results shown in Figure 6d. The Nyquist radii indicate that the electrical conductivities (i.e., inverse impedances) are in the order CeO_{2-x} < Mo-CeO_{2-x} < Ru-CeO_{2-x}. The strong demand of these *n*-type materials for electrons suggests that metal interstitials and F centers would act as electron traps. Also, the tendency for metal vacancies to exhibit midgap states near the VB suggests these defects also would not assist electron transfer.[14] However, the EPR data of Figure 3f are significant in that the signal for the *g* factor of 1.967 (3589 G) for Ru-CeO_{2-x} is significantly larger than that for Mo-CeO_{2-x}, which indicates a significant presence of unpaired electrons. Table 1 shows that the $[O–Ce^{3+}]$ for Ru-CeO_{2-x} is ≈40% greater than that for Mo-CeO_{2-x}. Therefore, it is clear that the unpaired electron associated with the Ce^{4+}/Ce^{3+} in the doped bulk of Ru-CeO_{2-x} is a probable cause of the greater electrical conductivity. However, Table S8 in the Supporting Information also shows that the BET surface area of Ru-CeO_{2-x} is ≈45% greater than that of Mo-CeO_{2-x}. Consequently, it is probable that the high electrical conductivity of Mo-CeO_{2-x} derives from combined surface and bulk electrical conductivities. The electrical conductivity of Mo-CeO_{2-x} is likely to be dominated by the surface while that of pure CeO_{2-x} is dominated by the bulk.

The similar slopes of the electrochemical surface area (ECSA) measurements in Figure S12a–d in the Supporting Information reveal that the concentrations of active sites for all three samples are similar. The data for the $V_{Ce}^{''''}$ active sites in Table 1 suggest that the slopes should be in the order CeO_{2-x} < Mo-CeO_{2-x} < Ru-CeO_{2-x}. However, there is very little difference between the slope, albeit they are in the order Mo-CeO_{2-x} < Ru-CeO_{2-x} ≈ CeO_{2-x}. These results support the previous conclusion that active sites do not play a dominant role and that the heterojunctions are primary.

Finally, it is noted that all three types of materials exhibit mesoporosity, which is of benefit to the mass transport required for hydrogen during electrochemical HER. However, the data in Table 1 reveal that the heterojunctions offer the further advantage of $V_{Ce}^{''''}$, which can act as sites for mass transport; they also feasibly can be used as sites for hydrogen storage.[73] In these cases, Ru-CeO_{2-x} would be more effective than Mo-CeO_{2-x} because the former has ≈60% greater $[V_{Ce}^{''''}]$.

The HER stability of the samples was tested by cyclic voltammetry (CV) for 1000 scans, the data for which are shown in Figure S13 in the Supporting Information. The current densities exhibit small declines after 1000 cycles in the order of CeO_{2-x} (0.11 mA cm^{-2}, 9.6%) < Mo-CeO_{2-x} (13.84 mA cm^{-2}, 15.3%) < Ru-CeO_{2x} (10.03 mA cm^{-2} 20.7%). Although CeO_{2-x} exhibits the highest HER activity retention, it is limited by its intrinsic low HER activity. These data suggest that the heterojunction lifetime is the limiting factor, where the superior performance of the chemisorbed Mo-CeO_{2-x} relative to that of the physisorbed Ru-CeO_{2-x} suggests that a possible cause of ultimate failure is heterojunction detachment.

SEM images before and after CV for 1000 scans, shown in Figure S14 in the Supporting Information, do not reveal any obvious nanostructural alteration of the samples. While Figure 2a–c suggests that there is little difference between the crystallites, the images of the 2D/3D flower-like nanosheets of CeO_{2-x} (Figure 1f,g), the heterojunction nanosheets (Figure 2n,p), and the powders deposited on the carbon-fiber paper (Figure S14, Supporting Information) show that the samples were different. The Mo-CeO_{2-x} consists of fragmented nanosheets with finely distributed MoO_3 (Figures 1f and 2n) while Ru-CeO_{2-x} consists of larger more coherent nanosheets with irregularly adsorbed RuO_2 (Figures 1g and 2o). These differences may be the cause of the different HER performances.

However, XPS testing before and after CV for 1000 scans of Mo-CeO_{2-x} reveals chemical alteration in the samples, as shown in Figure S15 in the Supporting Information. The XPS data for Ce 3d demonstrate that ultrasonication was sufficient to detach some of the chemisorbed heterojunctions, thereby eliminating the shielding of the surface Mo^{5+} and subsurface Mo^{4+} by the overlying heterojunction Mo^{6+}. These XPS data also show that the mixture of valence states before CV, which was Mo^{6+} (62 at%), Mo^{5+} (27 at%), and Mo^{4+} (11 at%) underwent oxidation to form a mixture of valence states after CV

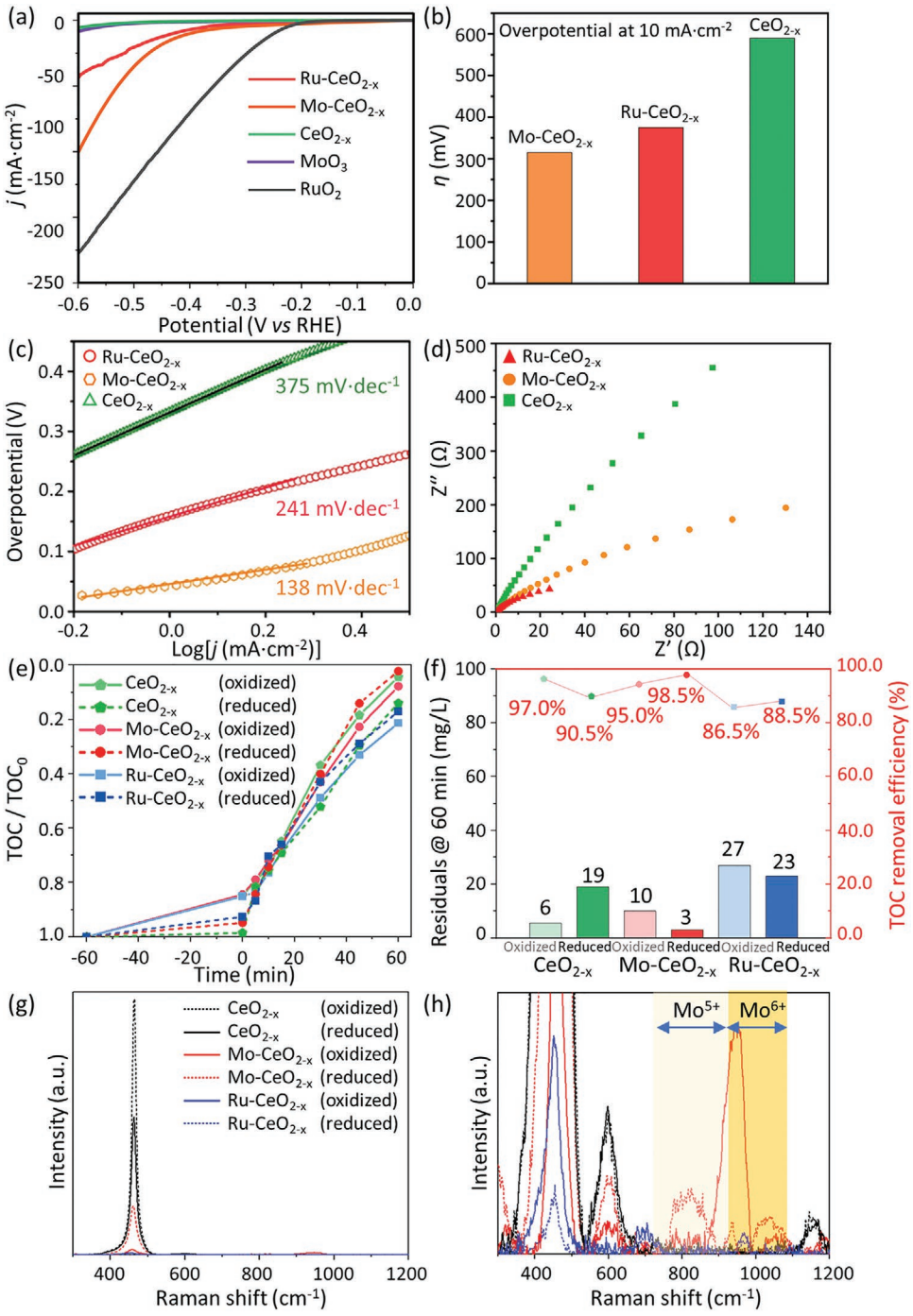

Figure 6. Electrocatalytic HER performance of CeO_{2-x}, Mo-CeO_{2-x}, Ru-CeO_{2-x}: a) Linear sweep voltammetry curves include MoO_3 and RuO_2 in 1 M H_2SO_4 (pH = 0) at scan rate of 5 mV s^{-1}; b) plot of the overpotential required to reach 10 mA cm^{-2}; c) Tafel plots for HER; d) electrochemical impedance spectroscopy (EIS) results. Catalytic ozonation of salicylic acid performance of CeO_{2-x}, Mo-CeO_{2-x}, and Ru-CeO_{2-x}: e) removal efficiency of salicylic acid before (–) and after (+) catalytic ozonation using samples before and after reduction: Reaction conditions: $[salicylic\ acid]_0$ = 200 mg L^{-1}; catalyst loading = 10 mg L^{-1}; oxygen flow rate = 750 mL min^{-1}; ozone concentration = 7 mg L^{-1} (TOC = total organic carbon); f) expanded plot of a) at 60 min; g) Raman spectra of the oxides before and after reduction, h) expanded plot of (g).

of Mo^{6+} (83 at%), Mo^{5+} (12 at%), and Mo^{4+} (5 at%). Since the $[Ce^{3+}]$ increased and the $[Mo^{5+}]$ decreased, this suggests that CV provided a driving force for IVCT according to the reverse of Equation (1). This may be a cause of the deterioration of the HER stability. These changes could improve the previously mentioned directional diffusion of charge carriers, charge separation, heterojunction bond strength, charge transfer between phases, and IVCT but they could worsen the heterojunction detachment and increase the potential for restacking of the nanosheets.

These materials also were examined for their performances in aqueous-phase catalytic ozonation of salicylic acid, which was as high as 98% removal of total organic carbon (TOC) after only 60 min. Figure 6e,f shows the TOC removal profiles of as-prepared (i.e., oxidized, and reduced samples). The atmospheres were altered in order to determine if Ce and/or Mo redox effects would occur. Since ozonation is facilitated in basic solutions[74] and the presence of Ce^{3+} also is enhanced in basic solutions,[75] then the [Ce^{3+}], which would be favored by reducing conditions, is likely to be an indicator of ozonation performance. However, Table 1 shows that the surface [Ce^{3+}] was the same for all three samples and the bulk [Ce^{3+}] was greatest for Ru-CeO_{2-x}, which exhibits the worst performance, as shown in Figure 6e (60 min). Further, while the heterojunctions confirmed superior ozonation after reduction, the reverse was the case for CeO_{2-x}.

Although it is well known that the presence of oxygen vacancies enhances the formation of reactive oxygen species (ROS) and radicals,[76] the present work shows that these defects have little effect on the equilibria. However, the presence of cation vacancies, which have charge opposite to that of oxygen vacancies, can be expected to annihilate ROS and radicals. Table 1 shows that the [V_{Ce}''''] was in the order CeO_{2-x} < Mo-CeO_{2-x} < Ru-CeO_{2-x}, which correlates inversely with the ozonation performance for oxidized samples. While the presence of positively charged solutes would be expected to act similarly to oxygen vacancies, the unknown nature of their precise surface distributions precludes conclusion.

There appear to be two effects that result from reduction. First, Figure 6e,f shows that the effect was minor for the two heterojunctions, but it was more significant for CeO_{2-x}. Since the Mo was limited to the surface and subsurface, the valence of Ru is very stable, and the Ce^{4+}/Ce^{3+} redox is well known, a larger effect for CeO_{2-x} is not surprising. However, the effect is the reverse of that expected, where the expected increase in [Ce^{3+}] from reduction should have improved the performance, which is not the case. Consequently, it is considered that the aggressive reducing conditions were sufficiently severe to have reduced the CeO_{2-x} to the point of initiating structural destabilization and partial amorphization, which is known to reduce catalytic performance.[77] Hence, for the two doped materials, the dominance of the Mo-CeO_{2-x} heterojunction allows it to act as a stabilizer while the extensive solid solubility for Ru-CeO_{2-x} acted similarly. Second, the ozonation performance was altered from that after oxidation, where the rankings after reduction were reversed for CeO_{2-x} and Mo-CeO_{2-x} (Ru-CeO_{2-x} remained the worst). The result is attributed to the role of IVCT on the Mo valences on the surface of Mo-CeO_{2-x}, although this effect decreased the residual TOC only from 4% to 2%. Figure 6g,h shows Raman spectra for the samples before and after reduction. The intensity changes in the Mo^{6+} and Mo^{5+} peaks and the defect concentrations from the ratios of the Raman peak areas are shown in Figure 6h. These data reveal that the introduction of Mo cations into the CeO_{2-x} structure results in slight surface tensile stress. The directions and extents of shift (Table S15, Supporting Information) are consistent with the extents of solid solubility (surface/subsurface vs bulk) and, as revealed by surface analysis by the Raman laser, residual surface tension arising from attraction between the dopant ion in the central interstice and the oxygen sublattice as well as the formation of large V_{Ce}''''. Further, the peak area ratios are consistent with, again, the extents of solid solubility (surface/subsurface vs bulk) and the associated defect densities.

3. Conclusions

The present work interprets the physicochemical properties and catalytic performance of novel free-standing CeO_{2-x}-based scaffolds that contain ultrathin holey 2D nanosheets and nanosheets decorated with heteroatoms of MoO_{3-x} and RuO_2. The heterojunctions were fabricated by strategizing band gap alignment and establishing control over the structural defects. Further, DFT simulations and atomic-scale characterization were applied for in-depth chemical and physical analysis, which highlighted the atomic-scale contributions of the TMO heteroatoms. The key conclusions from the present work are as follows:

CeO_{2-x}: The HER performance was the poorest of the three types of samples owing to the absence of a heterojunction nanostructure. The ozonation performance after oxidation was high owing to the effective absence of oxygen vacancies while the performance after reduction was poor owing to structural destabilization and associated partial amorphization from the aggressive reducing conditions.

Mo Doping: Mo exhibits low solid solubility (≈2.4 at%) in CeO_{2-x} and the solute distribution is limited to the surface and subsurface of the CeO_{2-x} nanosheet. Solubility occurs interstitially, which is supported by both experimental and DFT simulations. The band gap decreased slightly from 2.75 to 2.62 eV relative to CeO_{2-x} owing to the raising of the Fermi level to the proximity of the conduction band; this is attributed to the effect of the F centers and Mo interstitials. Moreover, IVCT results in a graded solubility region, with an inward gradient of $Mo^{6+} \rightarrow Mo^{5+} \rightarrow Mo^{4+}$ and this is responsible for the outstanding ozonation performance for reduced Mo-CeO_{2-x}. The ozonation performance for oxidized Mo-CeO_{2-x} was intermediate and correlates inversely with the cerium vacancy concentration. The HER performance is superior to that of other CeO_{2-x}-based catalysts owing to charge transfer through the high-density homogenously distributed small heterojunction particles strongly bonded by chemisorption and the valence-graded interface.

Ru Doping: Ru exhibits extensive solid solubility (≥6.8 at%) in CeO_{2-x} and the solute distribution is through the nanosheet bulk. The interstitial solubility mechanism is supported by both experimental and DFT simulations. The band gap decreased significantly from 2.75 to 1.75 eV relative to CeO_{2-x} owing to the raising of the Fermi level to above the conduction band; this is attributed to the F centers and Ru interstitials. The HER performance is inferior to that of Mo-CeO_{2-x} heterojunctions owing to the poor charge transfer through the low density of inhomogenously distributed large heterojunction particles weakly bonded by physisorption. Further, the ozonation performance for both oxidized and reduced Ru-CeO_{2-x} was poor, owing to high cerium vacancy concentration.

The present work shows that defect-sensitive analytical techniques and DFT can be interpreted in terms of defect equilibria and IVCT in order to synthesize a comprehensive mechanistic interpretation of the effects of solid solubility, charge

compensation, and defect formation on catalytic performance. Such mechanistic analyses can provide the bases for defect engineering aimed at the optimization of the functionalities of materials.

4. Experimental Section

All experimental details are included in the Supporting Information.

Supporting Information

Supporting Information is available from the Wiley Online Library or from the author.

Acknowledgements

The authors acknowledge financial support from the Australian Research Council (ARC Grant DP170104130) and the characterization facilities provided by the Mark Wainwright Analytical Centre at UNSW Sydney.

Conflict of Interest

The authors declare no conflict of interest.

Author Contributions

X.Z. undertook all of the experimental work, conducted characterization and data analysis, except the catalysis testing, wrote the initial draft of the manuscript, and worked on all subsequent drafts. S.S.M. designed the experimental program, worked on all subsequent drafts, and supervised the project. J.S., R.D., A.A.E.V. undertook the catalytic testing, wrote the associated preliminary data analysis, and worked on all subsequent drafts. C.C. undertook all of the DFT work, wrote the associated data analysis, and contributed to the final draft. Y.Y. assisted with acquisition of the AFM and KPFM data. S.L. assisted with acquisition of the TEM data. V.W. assisted with sample preparation. E.Y.C. and H.A. assisted with data analysis during the revision process, P.K. jointly supervised the project and worked on all subsequent drafts. C.C.S. jointly supervised the project, provided the basis for the formal data analysis, and worked on all subsequent drafts.

Data Availability Statement

The data that supports the findings of this study are available in the supplementary material of this article.

Keywords

2D, defects, heterojunctions, holey nanosheets, solid solubility

Received: April 1, 2021
Revised: June 1, 2021
Published online:

[1] L. E. Strange, J. Yadav, X. Li, S. Pan, *J. Electrochem. Soc.* **2020**, *167*, 146518.
[2] J. Su, G. D. Li, X. H. Li, J. S. Chen, *Adv. Sci.* **2019**, *6*, 1801702.
[3] T. S. Moss, C. Hilsum, *Handbook on Semiconductors*, Elsevier Science Publishers, Netherlands **1993**.
[4] H. Shi, C. Yan, X. Z. Chen, Z. Wang, T. Ouyang, M. L. Guo, Z. Q. Liu, *Appl. Catal. B* **2020**, *276*, 119138.
[5] Y. V. Kaneti, Q. M. Zakaria, Z. Zhang, C. Chen, J. Yue, M. Liu, X. Jiang, A. Yu, *J. Mater. Chem. A* **2014**, *2*, 13283.
[6] K. Q. Lu, Y. H. Li, F. Zhang, M. Y. Qi, X. Chen, Z. R. Tang, Y. M. Yamada, M. Anpo, M. Conte, Y. J. Xu, *Nat. Commun.* **2020**, *11*, 5181.
[7] T. C. Achee, W. Sun, J. T. Hope, S. G. Quitzau, C. B. Sweeney, S. A. Shah, T. Habib, M. J. Green, *Sci. Rep.* **2018**, *8*, 14525.
[8] T. W. Kang, J. Han, S. Lee, I. J. Hwang, S. J. Jeon, J. M. Ju, M. J. Kim, J. K. Yang, B. Jun, C. H. Lee, *Nat. Commun.* **2018**, *9*, 2549.
[9] A. Younis, D. Chu, Y. V. Kaneti, S. Li, *Nanoscale* **2016**, *8*, 378.
[10] X. Wu, X. Yu, Z. Huang, H. Shen, G. Jing, *Appl. Catal. B* **2020**, *268*, 118419.
[11] C. Huang, J. Dong, W. Sun, Z. Xue, J. Ma, L. Zheng, C. Liu, X. Li, K. Zhou, X. Qiao, *Nat. Commun.* **2019**, *10*, 2779.
[12] L. Wang, C. Shi, L. Pan, X. Zhang, J. J. Zou, *Nanoscale* **2020**, *12*, 4790.
[13] J. Xiong, J. Di, J. Xia, W. Zhu, H. Li, *Adv. Funct. Mater.* **2018**, *28*, 1801983.
[14] G. Bahmanrokh, C. Cazorla, S. S. Mofarah, R. Shahmiri, Y. Yao, I. Ismail, W. F. Chen, P. Koshy, C. C. Sorrell, *Nanoscale* **2020**, *12*, 4916.
[15] R. Schmitt, A. Nenning, O. Kraynis, R. Korobko, A. I. Frenkel, I. Lubomirsky, S. M. Haile, J. L. Rupp, *Chem. Soc. Rev.* **2020**, *49*, 554.
[16] X. Wu, Z. Chen, X. Yu, Z. Huang, H. Shen, G. Jing, *Chem. Eng. J.* **2020**, *399*, 125629.
[17] I. Saptiama, Y. V. Kaneti, Y. Suzuki, K. Tsuchiya, N. Fukumitsu, T. Sakae, J. Kim, Y. M. Kang, K. Ariga, Y. Yamauchi, *Small* **2018**, *14*, 1800474.
[18] C. Li, Q. Li, Y. V. Kaneti, D. Hou, Y. Yamauchi, Y. Mai, *Chem. Soc. Rev.* **2020**, *49*, 4681.
[19] M. Nolan, J. E. Fearon, G. W. Watson, *Solid State Ionics* **2006**, *177*, 3069.
[20] L. Zeng, Z. Cheng, J. A. Fan, L. S. Fan, J. Gong, *Nat. Rev. Chem.* **2018**, *2*, 349.
[21] H. L. Bohn, *Soil Sci.* **1971**, *112*, 39.
[22] Y. Xu, S. S. Mofarah, R. Mehmood, C. Cazorla, P. Koshy, C. C. Sorrell, *Mater. Horiz.* **2021**, *8*, 102.
[23] W. Hume-Rothery, G. W. Mabbott, K. M. Channel Evans, *Philos. Trans. R. Soc. London* **1934**, *233*, 1.
[24] O. A. Ustinov, G. P. Novoselov, M. A. Andrianov, N. T. Chebotarev, *Neorganicheskoj Khimii* **1970**, *15*, 2549.
[25] A. Aitbekova, L. Wu, C. J. Wrasman, A. Boubnov, A. S. Hoffman, E. D. Goodman, S. R. Bare, M. Cargnello, *J. Am. Chem. Soc.* **2018**, *140*, 13736.
[26] Y. Li, X. Wang, Y. Shao, D. Tang, B. Wu, Z. Tang, W. Lin, *Phys. Chem. Chem. Phys.* **2015**, *17*, 1156.
[27] L. Nie, D. Mei, H. Xiong, B. Peng, Z. Ren, X. I. P. Hernandez, A. DeLaRiva, M. Wang, M. H. Engelhard, L. Kovarik, A. D. Datye, *Science* **2017**, *358*, 1419.
[28] G. Lu, H. Zheng, J. Lv, G. Wang, X. Huang, *J. Power Sources* **2020**, *480*, 229091.
[29] H. Ren, P. Koshy, W. F. Chen, S. Qi, C. C. Sorrell, *J. Hazard. Mater.* **2017**, *325*, 340.
[30] L. Zhou, X. Li, Z. Yao, Z. Chen, M. Hong, R. Zhu, Y. Liang, J. Zhao, *Sci. Rep.* **2016**, *6*, 23900.
[31] A. Chen, X. Yu, Y. Zhou, S. Miao, Y. Li, S. Kuld, J. Sehested, J. Liu, T. Aoki, S. Hong, M. F. Camellone, *Nat. Catal.* **2019**, *2*, 334.
[32] V. Kumar, W. F. Chen, X. Zhang, Y. Jiang, P. Koshy, C. C. Sorrell, *Ceram. Int.* **2019**, *45*, 22085.
[33] G. Korotcenkov, *Cerium Oxide (CeO_2): Synthesis, Properties and Applications*, Elsevier, USA **2019**.

[34] S. S. Mofarah, E. Adabifiroozjaei, R. Pardehkhorram, M. H. N. Assadi, M. Hinterstein, Y. Yao, X. Liu, M. B. Ghasemian, K. Kalantar-Zadeh, R. Mehmood, C. Cazorla, R. Shahmiri, G. Bahmanrokh, S. Bhattacharyya, M. C. Spadaro, J. Arbiol, S. Lim, Y. Xu, H. Arandiyan, J. Scott, P. Koshy, C. C. Sorrell, *Adv. Mater.* **2019**, *31*, 1905288.
[35] W. F. Chen, H. Chen, P. Koshy, A. Nakaruk, C. C. Sorrell, *Mater. Chem. Phys.* **2018**, *205*, 334.
[36] K. W. Böer, *Survey of Semiconductor Physics*, Wiley, Ann Arbor, MI **2002**.
[37] A. F. Henriksen, W. D. Kingery, *Ceramurgia Int.* **1979**, *5*, 11.
[38] E. Sartoretti, C. Novara, F. Giorgis, M. Piumetti, S. Bensaid, N. Russo, D. Fino, *Sci. Rep.* **2019**, *9*, 3875.
[39] Y. Lee, G. He, A. J. Akey, R. Si, M. Flytzani-Stephanopoulos, I. P. Herman, *J. Am. Chem. Soc.* **2011**, *133*, 12952.
[40] A. Filtschew, K. Hofmann, C. Hess, *J. Phys. Chem. C* **2016**, *120*, 6694.
[41] M. Dosa, M. Piumetti, S. Bensaid, T. Andana, C. Novara, F. Giorgis, D. Fino, N. Russo, *Catal. Lett.* **2018**, *148*, 298.
[42] W. F. Chen, P. Koshy, C. C. Sorrell, *Int. J. Hydrogen Energy* **2015**, *40*, 16215.
[43] L. Brewer, R. H. Lamoreaux, *Bull. Alloy Phase Diagrams* **1980**, *1*, 85.
[44] A. A. Gusev, E. G. Avvakumov, A. Medvedev, A. I. Masliy, *Sci. Sintering* **2007**, *39*, 51.
[45] C. C. Mardare, A. W. Hassel, *Phys. Status Solidi A* **2019**, *216*, 1900047.
[46] J. Wang, N. Umezawa, H. Hosono, *Adv. Energy Mater.* **2016**, *6*, 1501190.
[47] R. T. Shannon, C. T. Prewitt, *Acta Crystallogr., Sect. B: Struct. Sci., Cryst. Eng. Mater.* **1969**, *25*, 925.
[48] S. S. Mofarah, E. Adabifiroozjaei, Y. Yao, P. Koshy, S. Lim, R. Webster, X. Liu, R. K. Nekouei, C. Cazorla, Z. Liu, Y. Wang, N. Lambropoulos, C. C. Sorrell, *Nat. Commun.* **2019**, *10*, 2594.
[49] R. Raman, A. Shukla, A. Gayen, M. Hegde, K. Priolkar, P. Sarode, S. Emura, *J. Power Sources* **2006**, *157*, 45.
[50] E. Paparazzo, G. Ingo, N. Zacchetti, *J. Vac. Sci. Technol.* **1991**, *9*, 1416.
[51] K. I. Maslakov, Y. A. Teterin, A. J. Popel, A. Y. Teterin, K. E. Ivanov, S. N. Kalmykov, V. G. Petrov, P. K. Petrov, I. Farnan, *Appl. Surf. Sci.* **2018**, *448*, 154.
[52] D. G. Cheng, M. Chong, F. Chen, X. Zhan, *Catal. Lett.* **2008**, *120*, 82.
[53] M. Krawczyk, M. Holdynski, W. Lisowski, J. Sobczak, A. Jablonski, *Appl. Surf. Sci.* **2015**, *341*, 196.
[54] B. Choudhury, M. Dey, A. Choudhury, *Int. Nano Lett.* **2013**, *3*, 25.
[55] J. M. Costantini, S. Miro, N. Touati, L. Binet, G. Wallez, G. Lelong, M. Guillaumet, W. J. Weber, *J. Appl. Phys.* **2018**, *123*, 025901.
[56] W. D. Kingery, *J. Am. Ceram. Soc.* **1974**, *57*, 1.
[57] E. Abi-Aad, A. Bennani, J.-P. Bonnelle, A. Aboukaïs, *J. Chem. Soc.* **1995**, *91*, 99.
[58] R. Rakhmatullin, V. Semashko, S. Korableva, A. Kiiamov, A. A. Rodionov, R. Tschaggelar, J. A. van Bokhoven, C. Paun, *Mater. Chem. Phys.* **2018**, *219*, 251.
[59] J. Wang, E. Gürdal, A. Horneber, S. Dickreuter, S. Kostcheev, A. J. Meixner, M. Fleischer, P.-M. Adam, D. Zhang, *Nanoscale* **2018**, *10*, 8240.
[60] S. Aškrabić, Z. Dohčević-Mitrović, V. Araújo, G. Ionita, M. M. de Lima Jr., A. Cantarero, *J. Phys. D: Appl. Phys.* **2013**, *46*, 495306.
[61] S. S. Mofarah, E. Adabifiroozjaei, Y. Wang, H. Arandiyan, R. Pardehkhorram, Y. Yao, M. H. N. Assadi, R. Mehmood, W. F. Chen, C. Tsounis, J. Scott, S. Lim, R. Webster, V. Zhong, Y. Xu, P. Koshy, C. C. Sorrell, *J. Mater. Chem. A* **2020**, *8*, 4753.
[62] G. Allaedini, S. M. Tasirin, *Asian J. Nanosci. Mater.* **2019**, *2*, 421.
[63] V. R. PaiVerneker, A. N. Petelin, F. J. Crowne, D. C. Nagle, *Phys. Rev. B* **1989**, *40*, 8555.
[64] H. B. Michaelson, *J. Appl. Phys.* **1977**, *48*, 4729.
[65] E. Kusmierek, *Catalysts* **2020**, *10*, 1435.
[66] M. Baldoni, L. Craco, G. Seifert, S. Leoni, *J. Mater. Chem. A* **2013**, *1*, 1778.
[67] N. Mehtougui, D. Rached, R. Khenata, H. Rached, M. Rabah, S. Bin-Omran, *Mater. Sci. Semicond. Process.* **2012**, *15*, 331.
[68] L. L. Kelly, D. A. Racke, P. Schulz, H. Li, P. Winget, H. Kim, P. Ndione, A. K. Sigdel, J. L. Bredas, J. J. Berry, S. Graham, *J. Phys.: Condens. Matter* **2016**, *28*, 094007.
[69] M. M. Khan, W. Khan, M. Ahamed, A. N. Alhazaa, *Sci. Rep.* **2017**, *7*, 12560.
[70] T. Shinagawa, A. T. Garcia-Esparza, K. Takanabe, *Sci. Rep.* **2015**, *5*, 13801.
[71] Y. Hou, J. Wang, C. Hou, Y. Fan, Y. Zhai, H. Li, F. Dang, S. Chou, *J. Mater. Chem. A* **2019**, *7*, 6552.
[72] P. Gao, Z. Chen, Y. Gong, R. Zhang, H. Liu, P. Tang, X. Chen, S. Passerini, J. Liu, *Adv. Energy Mater.* **2020**, *10*, 1903780.
[73] B. P. Hahn, J. W. Long, D. R. Rolison, *Acc. Chem. Res.* **2013**, *46*, 1181.
[74] J. Nawrocki, B. Kasprzyk-Hordern, *Appl. Catal. B* **2010**, *99*, 27.
[75] B. Bouchaud, J. Balmain, G. Bonnet, F. Pedraza, *J. Rare Earths* **2012**, *30*, 559.
[76] A. A. Esmailpour, S. Moradi, J. Yun, J. Scott, R. Amal, *Catal. Sci. Technol.* **2019**, *9*, 5979.
[77] D. A. Hanaor, C. C. Sorrell, *J. Mater. Sci.* **2011**, *46*, 855.